Geophysical Journal International

Geophys. J. Int. (2024) **237,** 288–301
Advance Access publication 2024 February 05
GJI Geodynamics and Tectonics

https://doi.org/10.1093/gji/ggae046

Constraints from GPS measurements on plate coupling within the Makran subduction zone and tsunami scenarios in the western Indian Ocean

Guo Cheng [1,2,*] William D. Barnhart[3] and David Small[4]

[1]*Department of Earth and Environmental Sciences, University of Iowa, Iowa City, IA* 52242, *USA E-mail: gcheng@unr.edu*
[2]*Department of Earth & Planetary Sciences, University of California Santa Cruz, Santa Cruz, CA* 95064, *USA*
[3]*U.S. Geological Survey, Earthquake Hazards Program, Golden, CO* 80401, *USA*
[4]*Department of Earth Sciences, University of Oregon, Eugene, OR* 97403, *USA*

Accepted 2024 February 1. Received 2023 December 8; in original form 2023 May 26

SUMMARY

Plate-coupling estimates and previous seismicity indicate that portions of the Makran megathrust of southern Pakistan and Iran are partially coupled and have the potential to produce future magnitude 7+ earthquakes. However, the GPS observations needed to constrain coupling models are sparse and lead to an incomplete understanding of regional earthquake and tsunami hazard. In this study, we assess GPS velocities for plate coupling of the Makran subduction zone with specific attention to model resolution and the accretionary prism rheology. We use finite element model-derived Green's functions to invert for the interseismic slip deficit under both elastic and viscoelastic Earth assumptions. We use the model resolution matrix to characterize plate-coupling scenarios that are consistent with the limited spatial resolution afforded by GPS observations. We then forward model the corresponding tsunami responses at major coastal cities within the western Indian Ocean basin. Our plate-coupling results show potential segmentation of the megathrust with varying coupling from west to east, but do not rule out a scenario where the entire length of the megathrust could rupture in a single earthquake. The full subduction zone rupture scenarios suggest that the Makran may be able to produce earthquakes up to M_w 9.2. The corresponding tsunami model from the largest earthquake event (M_w 9.2) estimates maximum wave heights reaching 2–5 m at major port cities in the northern Arabian Sea region. Cities on the west coast of India are less affected (1–2 m). Coastlines bounding eastern Africa, and the Strait of Hormuz, are the least affected (<1 m).

Key words: Satellite geodesy; Seismic cycle; Indian Ocean; Inverse theory; Earthquake hazards; Tsunamis.

1 INTRODUCTION

The Makran subduction zone (MSZ) of Iran and Pakistan currently accommodates northward subduction of the Arabian oceanic plate beneath continental Eurasia at a rate of ∼3.5 cm yr^{-1} over the last 3 Ma (Kopp *et al.* 2000; DeMets *et al.* 2010; Smith *et al.* 2012; Fig. 1). The MSZ stretches approximately 1000 km from west to east and is bounded by strike-slip fault systems: the right-lateral Minab–Zendan fault to the west and the left-lateral Ornach-Nal and Chaman faults to the east. These two strike-slip systems separate the Makran region from active continent–continent collisions forming the Himalaya and Zagros Mountain ranges. The distance between the active trench and volcanic arc in the MSZ varies from 400 to 600 km, owing to a shallow subduction angle (<5°; Quittmeyer & Jacob 1979; Byrne *et al.* 1992; Regard *et al.* 2010; Barnhart *et al.* 2014; Hayes *et al.* 2018). The active convergence between the Arabian and Eurasian plates also produces the world's largest accretionary prism in the MSZ, the Makran accretionary prism, which is divided into a 100–150 km wide submarine portion and a 150–200 km subaerial portion from south to north, respectively (Burg 2018). The notable width of the emergent portion of the accretionary prism likely results from shallow angle subduction, exceptionally high incoming sediment thickness (up to 7.5 km) at the trench (Smith *et al.* 2012) and extensive sediment underplating, evidenced by reflection seismic data (Fowler *et al.* 1985; Platt *et al.* 1985; Kopp *et al.* 2000).

Historically, the MSZ shows relatively low seismicity rates in comparison to other subduction zones in the world (Heidarzadeh

*Now at: Nevada Bureau of Mines and Geology, University of Nevada, Reno, NV, USA.

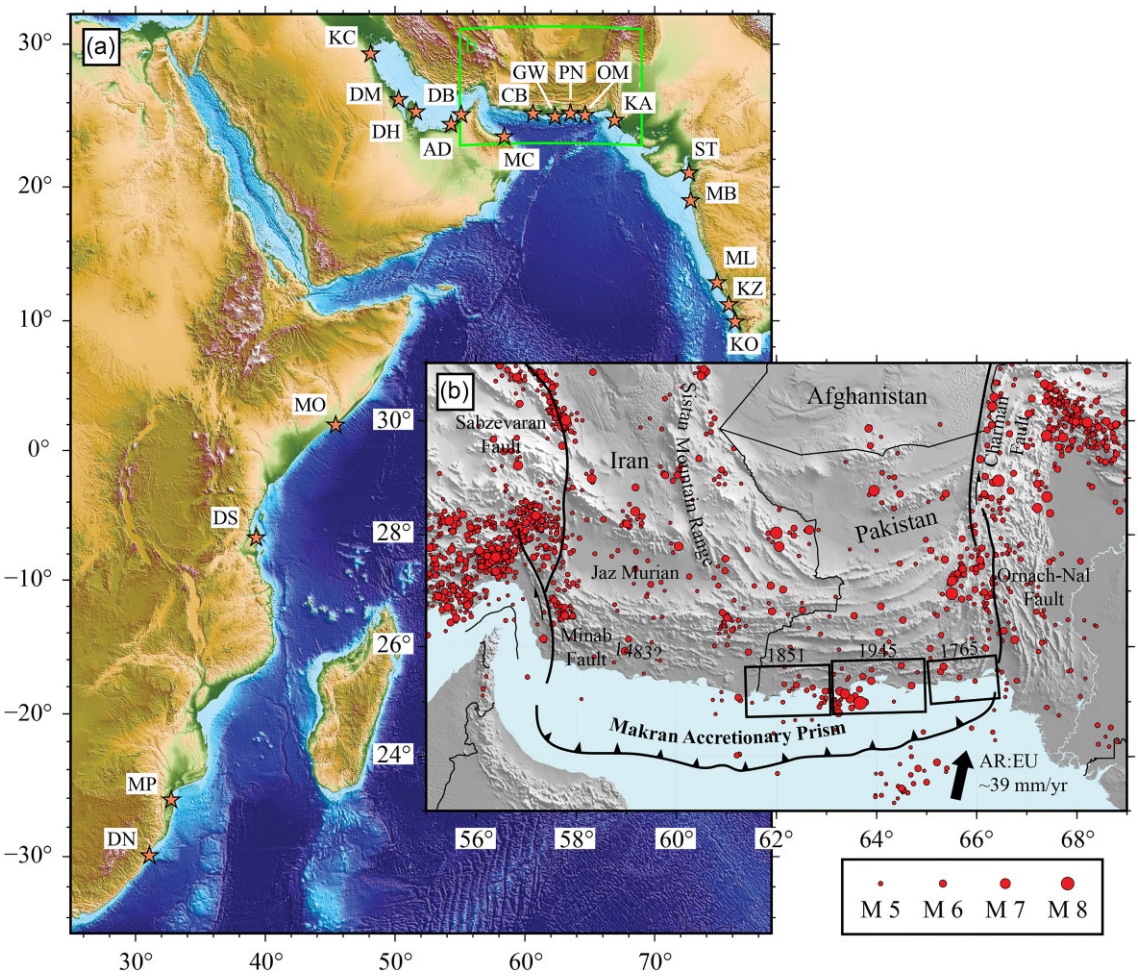

Figure 1. (a) Topographic and bathymetric map of the western Indian Ocean region. Orange stars indicate major coastal cities: MC: Muscat; CB: Chah Bahar; GW: Gwadar; PN: Pasni; OM: Ormara; KA: Karachi; ST: Surat; MB: Mumbai; ML: Mangalore; KZ: Kozhikode; KO: Kochi; KC: Kuwait City; DM: Dammam; DH: Doha; AD: Abu Dhabi; DB: Dubai; MO; Mogadishu; DS: Dar es Salaam; MP: Maputo; DN: Durban. (b) Regional seismicity (M_w 4.5+, 1905–2022) and simplified structural map of the Makran subduction zone, modified from Burg (2018). Three rectangles along the coastal Makran indicate maximum estimated rupture areas for historic earthquake events (Byrne *et al.* 1992). Plate motion of Arabia relative to Eurasia (AR:EU) is shown by the solid arrow (DeMets *et al.* 2010). Structures and images are overlain on SRTM15+ relief model (Tozer *et al.* 2019).

et al. 2008; Mokhtari *et al.* 2019). However, several significant earthquakes have been reported in the MSZ, some of which were tsunamigenic. According to Byrne *et al.* (1992), four large earthquakes ($M_w > 7.0$) may have ruptured the plate boundary along the eastern part of the MSZ (Fig. 1), including the 1765 event that was felt strongly at Karachi in easternmost Makran, two coastal events in 1851 and 1864 affecting the town of Gwadar and the 1945 M_w 8.0–8.3 event near Pasni that was followed by a large aftershock in 1947 to the south. The 1945 event is the largest instrumentally recorded earthquake in the subduction zone and is known to have caused a large tsunami, which is possibly the second deadliest tsunami event in the Indian Ocean basin killing over 4000 people (Heck 1947). The western section of the Makran, in contrast, has less documented seismic activity than the eastern MSZ and holds no clearly documented record of great subduction zone earthquakes. Only two events are reported to have occurred in the western Makran, in 1008 and 1483, but the latter event likely occurred within the Strait of Hormuz and thus may not be associated with megathrust rupture (Musson 2009; Rajendran *et al.* 2013). Additionally, some non-megathrust earthquakes of the Makran were tsunamigenic, such as the 2013 Baluchistan strike-slip earthquake (M_w 7.7), which triggered a landslide offshore Makran and led to a tsunami event (Baptista *et al.* 2020; Heidarzadeh & Satake 2015; Hoffmann *et al.* 2015).

Several megacities are located along the rim of the western Indian Ocean (Fig. 1). These cities include Mumbai (18+ million), Karachi (16+ million), Surat (6+ million), Dar es Salaam (6+ million), Mogadishu (2+ million) and major cities in the Persian Gulf (such as Dubai, Kuwait City and Doha, each with a population exceeding 2 million). Therefore, tsunamigenic earthquakes produced by the MSZ will potentially lead to high economic losses and human casualties in the western Indian Ocean, making assessment of the earthquake and tsunami potential of the Makran a critical component of regional risk analysis. Several plate-coupling models (i.e. the degree of interseismic strain accumulation) of the Makran have been proposed by previous studies. For example, Frohling & Szeliga (2016) found that the Makran megathrust is segmented, with a plate coupling of 58 per cent in eastern and western Makran, and a lower coupling ratio (31 per cent) along the central-western portion of the Makran. Lin *et al.* (2015) conducted Bayesian inversion of interferometric synthetic aperture radar (InSAR) observations from 2003 to 2010 for plate-coupling model in the eastern MSZ. They showed that high interseismic coupling occurs in the ruptured area of the 1945 M_w 8.0–8.3 earthquake (Fig. 1), while lower coupling

lies on both sides of the epicentral area. The inferred plate-coupling model may imply future occurrence of magnitude 7+ earthquakes, or a multisegment rupture event that would likely exceed magnitude 8 (Lin *et al.* 2015).

These previous plate-coupling studies in the MSZ invoked an elastic half-space mechanical model (Okada 1992), where the Earth behaves elastically during the interseismic period. However, in a viscoelastic Earth, the stresses induced by megathrust coupling are relaxed through viscous flow in the mantle during the decades to centuries long interseismic period (Wang *et al.* 2012). Several studies have revealed that the elastic Earth assumption tends to overestimate plate coupling in subduction zone setting as it ignores the effects introduced by viscous flow within the mantle wedge. Li *et al.* (2015, 2018) conducted finite element modelling (FEM) to find that a purely elastic subduction zone model tends to overestimate the true coupling depth in North Chile and Cascadia. Li *et al.* (2020) showed that the assumption of a fully relaxed mantle may lead to underestimations of the coupling depth and/or plate coupling when ignoring the interseismic mantle relaxation. Furthermore, besides mantle viscoelasticity, simulations of post-seismic deformation following the 2013 Baluchistan earthquake show that the lower Makran accretionary wedge (12+ km depth) may undergo low-temperature viscoelastic deformation as well (Peterson *et al.* 2018; Cheng *et al.* 2022). Here, we conduct inversions of the GPS velocity data from Frohling & Szeliga (2016) for megathrust plate coupling of the MSZ using an FEM-derived Green's function under both elastic and viscoelastic Earth assumptions. We utilize the model resolution matrix derived from the Green's function to explore possible plate-coupling scenarios that the GPS observations could resolve. We then generate several megathrust earthquake scenarios based on these plate-coupling models and use them to forward model the corresponding tsunami responses at major coastal cities within the Persian Gulf, Arabian Sea and western Indian Ocean basin. The main goal of this study is to explore the population of subduction zone coupling scenarios, and by extension earthquake and tsunami scenarios, which are consistent with but incompletely resolved by the sparse geodetic observations currently available in the Makran.

2 INTERSEISMIC PLATE-COUPLING INVERSION

2.1. Interseismic plate coupling: inversion and model resolution

Our analysis of coupling in the Makran focuses on modelling the resolution afforded by sparse campaign GPS measurements made prior to the 2013 M_w7.7 Baluchistan earthquake that occurred within the sub-aerial accretionary prism. We first use the fixed Eurasia GPS velocities from Frohling & Szeliga (2016) to invert for interseismic back-slip rate on the Makran megathrust. The back-slip model (Savage 1983) assumes that interseismic velocities or displacements reflect deformation due to coupling between two plates, such that the back-slip rate can be related to the magnitude of a slip deficit accrued on the plate interface that can later be released in an earthquake. Therefore, the slip deficit caused by fault coupling can be modelled as fault slip in the opposite sense to the coseismic slip (back-slip). The plate coupling is then defined as the ratio between back-slip rate during the modelled period, and the plate convergence rate at the trench. 11 out of 19 GPS stations from Frohling & Szeliga (2016) are used for the back-slip rate inversion (Fig. 1). The remaining eight stations lie either to the east or west of the MSZ where deformation is likely influenced by the strike-slip motion of the transverse fault systems. The GPS station coordinates and velocities were estimated using the GAMIT/GLOBK analysis package (Herring *et al.* 2010a,b). Station coordinates and velocities were tied to the ITRF2008 global reference frame (Altamimi *et al.* 2011). The GPS velocities were rotated with respect to a fixed Eurasia reference frame using the pole-of-rotation parameters published in Altamimi *et al.* (2012).

We conduct the back-slip rate inversion based on a linear viscoelastic Makran accretionary prism model. The inverse problem describes the linear relationship between the back-slip rates on different fault patches and the surface displacement rates (i.e. GPS velocities) in the late stage of the interseismic period, when the post-seismic deformation from the previous large earthquake has diminished, and the surface deformation mainly results from interseismic megathrust loading. Thus, the inverse problem to solve for back-slip rate can be expressed as the linear system:

$$\boldsymbol{Gm} = \boldsymbol{d}, \tag{1}$$

where $\boldsymbol{G}$ is the matrix of Green's functions relating unit back-slip rate on a fault patch at depth to velocities at a free surface, $\boldsymbol{m}$ is the unsolved back-slip rate vector and $\boldsymbol{d}$ is the data vector that contains the noisy GPS velocities. Following Barnhart & Lohman (2010), we apply least-squares inversion to solve for $\boldsymbol{m}$, regularized by a minimum moment operator $\boldsymbol{L}$, which minimizes slip on any given fault patch irrespective of the behaviour of adjacent patches. The regularized least-squares inversion minimizes the norm of

$$\min \left\| \begin{bmatrix} \boldsymbol{G} \\ \lambda \boldsymbol{L} \end{bmatrix} \boldsymbol{m} - \begin{bmatrix} \boldsymbol{d} \\ 0 \end{bmatrix} \right\|, \tag{2}$$

where $\boldsymbol{L}$ is an identity matrix, and λ is a weighting parameter that adjusts the degree to which the inversion is regularized. This regularization scheme is different from a spatial regularization scheme such as a Laplacian smoothing matrix. Therefore, the inverted slip distribution is not necessarily expected to be 'smooth' (i.e. constant spatial gradient between slip asperities). We compared the inversion results using minimum moment and Laplacian regularizations and found that due to the sparse distribution of the GPS stations, the Laplacian regularization introduces unrealistically high back-slip rate asperities downdip of the regional seismogenic zone (Supporting Information Fig. S1). We explore the inversion results based on different λ values (Supporting Information Fig. S2) and choose the best-fit λ value by identifying the corner of the L-curve (Harris & Segall 1987).

We construct the $\boldsymbol{G}$ matrix using FEM-derived Green's functions, following Masterlark (2003). We use the finite element meshing software *Coreform-Cubit* (https://coreform.com/) to construct a layered viscoelastic 3-D subduction model, which is constrained by geophysical slab geometry (Craig & Copley 2014; Hayes *et al.* 2018), and material domains estimated from forward modelling of post-seismic deformation of the 2013 Baluchistan earthquake (Peterson *et al.* 2018; Cheng *et al.* 2022). The mesh geometry consists of four domains (Fig. 2): (1) an elastic upper wedge that extends to 12-km depth; (2) a Maxwell viscoelastic lower wedge that extends to a maximum depth of 40 km, which is the Moho depth reported in this region (Maggi *et al.* 2000; Shad Manaman *et al.* 2011; Abdollahi *et al.* 2018); (3) a 30 km thick elastic Arabian oceanic slab with megathrust geometry from the Slab2 model (Craig & Copley 2014; Hayes *et al.* 2018); and (4) a Maxwell viscoelastic oceanic and continental mantle at depths. To increase computational efficiency,

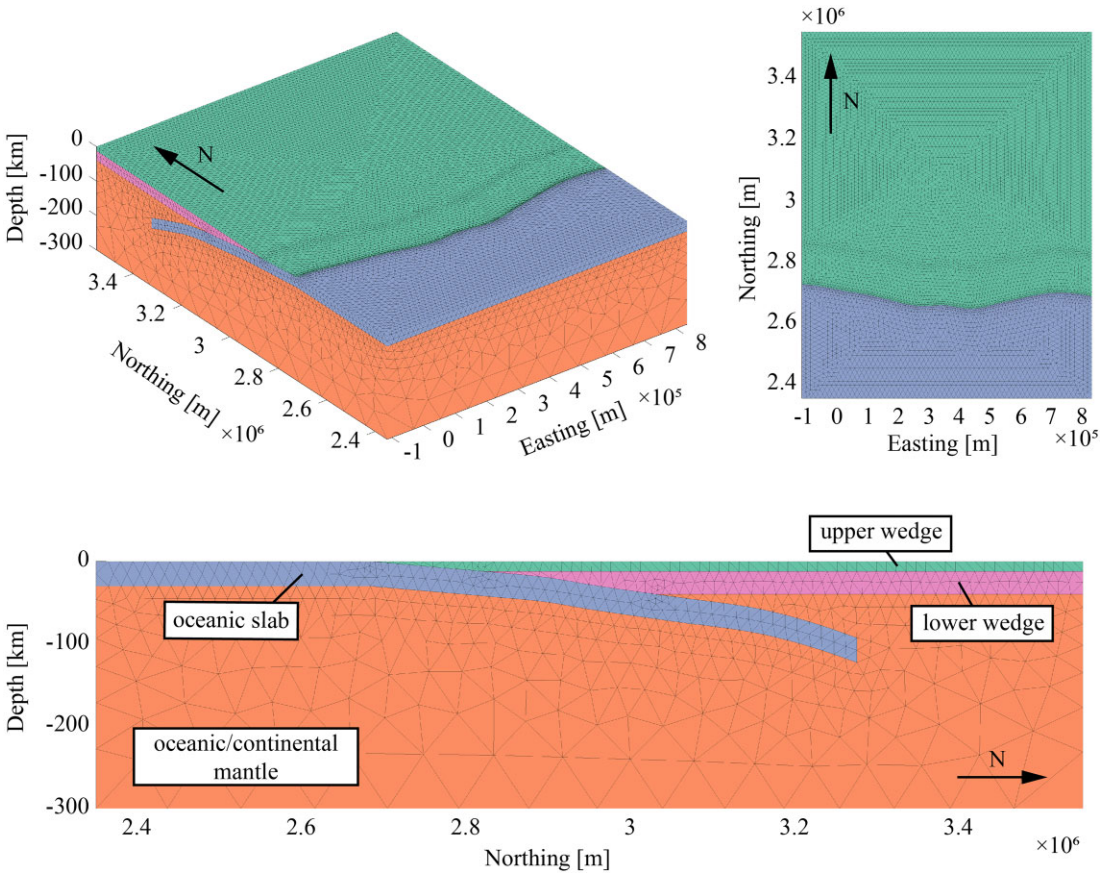

Figure 2. Makran subduction zone geometry and finite element mesh. Green domain: upper wedge. Blue domain: oceanic slab. Pink domain: lower wedge. Orange domain: oceanic and continental mantle.

instead of using the full megathrust mesh (10 350 patches in total), we discretize the plate interface into nonoverlapping patches with ∼30 km spacing (470 patches in total, Supporting Information Fig. S3). Each patch consists of sub-patches with a size on the scale of ∼15 km. We use open-source FEM software PyLith to assign material properties and derive the Green's functions (Aagaard *et al.* 2013). The materials properties for each domain are summarized in Supporting Information Table S1. We set free displacement boundary condition at the ground surface. We fixed the displacements to be zero in the horizontal directions along the northern/southern boundaries and set the eastern/western boundaries to be free. We then prescribe unit back-slip rate (1 m yr^{-1}) along strike and dip directions on one fault patch while keeping the slip rate zero on the remaining patches, and drive the simulation for 200 yr. The 200-yr simulation period is considerably longer than the Maxwell relaxation time of the viscoelastic materials (8 yr for the lower wedge, 50 yr for the mantle), which is an indication that the viscoelastic relaxation has stabilized and the simulation has reached the late stage of the interseismic period (Hu *et al.* 2004; Li *et al.* 2015). Additionally, we ignore any bias in the GPS velocity data that may be introduced by the prolonged post-seismic deformation of the 1945 Makran earthquake. For large (M > 8.5) subduction zone earthquakes, Li & Chen (2023) estimated the post-seismic phase to be in the range of 0.2–0.4 of their recurrence intervals. In the Makran region, the average recurrence time for magnitude 8 + earthquake is about 100–250 yr (Page *et al.* 1979). Therefore, although the post-seismic relaxation of the 1945 event may contribute to the GPS observations, we posit that this effect is small and the observed GPS velocities result solely from interseismic strain accumulation on the megathrust. We repeat the simulation process for every fault patch and calculate the surface velocities at the last time step, which are then flattened into column vectors and appended to the $\boldsymbol{G}$ matrix. For the elastic model, we calculate the $\boldsymbol{G}$ matrix following the same procedure as the viscoelastic model, but setting the material properties of the lower wedge and mantle domains to be elastic (Supporting Information Table S1).

After obtaining $\boldsymbol{G}$, we solve for the back-slip rate vector $\boldsymbol{m}$ (eq. 3). We fix the rake to be 110°, a slip direction that both best explains the GPS observations based on a grid search procedure (Supporting Information Fig. S4) and the relative plate motion resolved onto the subduction zone interface. We force the solution to be positive (slip along rake) and set the maximum allowable back-slip rate on each patch to be the plate convergence rate at the trench (fixed Eurasia reference frame, Altamimi *et al.* 2012). The regularized least squares solution can be written as

$$\boldsymbol{m}_{\text{est}} = \left(\begin{bmatrix} \boldsymbol{G} \\ \lambda \boldsymbol{L} \end{bmatrix}^T * \begin{bmatrix} \boldsymbol{G} \\ \lambda \boldsymbol{L} \end{bmatrix} \right)^{-1} \boldsymbol{G}^T \boldsymbol{d}, \tag{3}$$

where $\boldsymbol{m}_{\text{est}}$ is the estimated back-slip rate model. For each fault patch, we divide the interseismic back-slip rate model by the plate convergence rate at the trench to calculate the plate coupling. We translate the back-slip rate of each fault patch into the locking ratio by dividing the back-slip rate by the plate motion rate expected at the depth of each fault patch (Altamimi *et al.* 2012). We propagate the noise covariance structure of the data through the inversion and

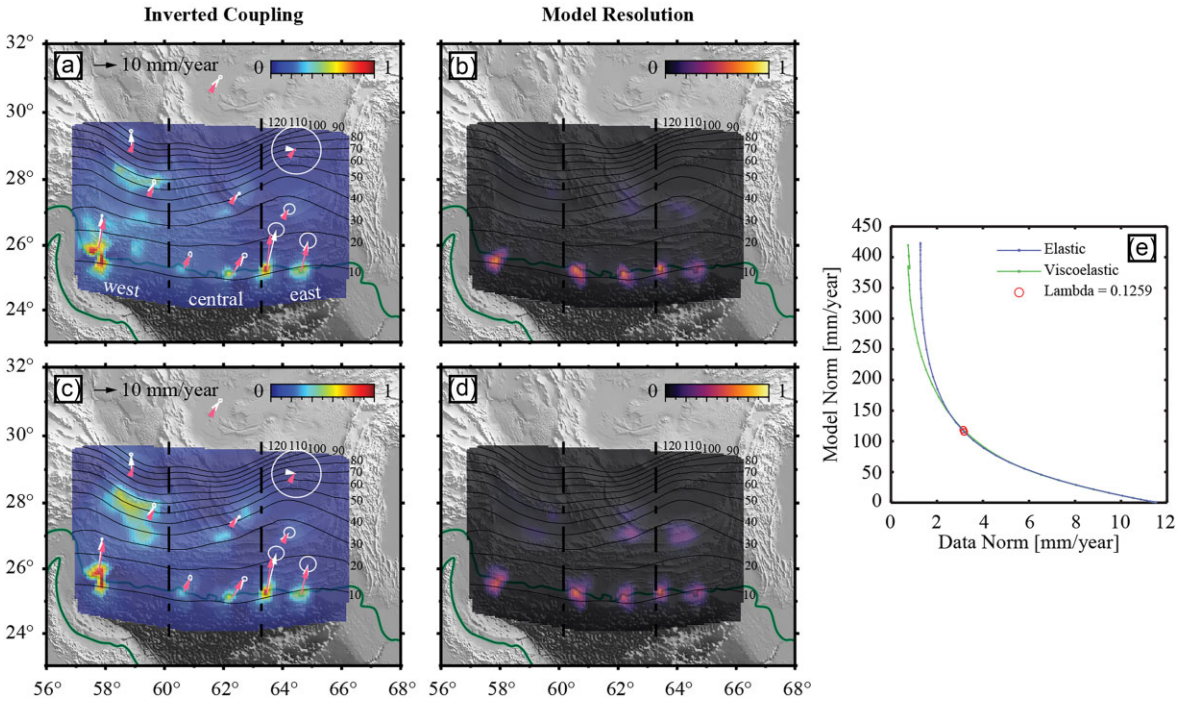

Figure 3. Inverted interseismic plate-coupling models and the diagonal components of the model resolution matrices of the Makran megathrust resulting from (a and b) viscoelastic model and (c and d) elastic model. (e) L-curve between the fit to data (data norm) and the model size (model norm), and the selected corner (λ) for each coupling model. White arrows: GPS velocity data from Frohling & Szeliga (2016); pink arrows: forward-predicted velocities from the inversion; black solid lines: contours of the plate interface marked by depth in kilometer; black dash lines: boundaries between different fault segments; dark green lines: coastlines.

eq. (3) becomes:

$$\boldsymbol{m}_{\text{est}} = \left(\begin{bmatrix} \boldsymbol{Ch} * \boldsymbol{G} \\ \lambda \boldsymbol{L} \end{bmatrix}^T * \begin{bmatrix} \boldsymbol{Ch} * \boldsymbol{G} \\ \lambda \boldsymbol{L} \end{bmatrix} \right)^{-1} [\boldsymbol{Ch} * \boldsymbol{G}]^T [\boldsymbol{Ch} * \boldsymbol{d}], \quad (4)$$

where $\boldsymbol{Ch}$ is the inverse Cholesky factorization of the data covariance structure (Harris & Segall 1987).

2.2. Interseismic plate-coupling inversion: results

Fig. 3 shows the plate-coupling inversion results, as well as the model resolution matrices for elastic and viscoelastic models. The model resolution matrix ($\boldsymbol{R}_{\text{m}}$) is defined as

$$\boldsymbol{R}_{\text{m}} = \left(\begin{bmatrix} \boldsymbol{G} \\ \lambda \boldsymbol{L} \end{bmatrix}^T * \begin{bmatrix} \boldsymbol{G} \\ \lambda \boldsymbol{L} \end{bmatrix} \right)^{-1} \boldsymbol{G}^T \boldsymbol{G} \quad (5)$$

and reflects the degree of spatial averaging the inverted model has over the underlying true model (Menke 2018). To a first order, despite differences in the deeper part of the fault (below 20-km depth), both elastic and viscoelastic models exhibit similar magnitude and spatial distribution of plate coupling in the shallow portion (Figs 3a and c), which likely results from the lack of GPS data in the region to capture the viscoelastic effects. According to Li *et al.* (2015, 2018), viscoelastic subduction zone behaviours affect interseismic deformation over longer spatial wavelength than simple elastic half-space models and thus dominate in the GPS signals further inland from the trench. Therefore, the lack of GPS stations in inland Makran may cause the inversion results from the viscoelastic model to be indistinguishable from the elastic model.

For both models, five regions with relatively high magnitudes of coupling are observed along strike at about 10-km depth. These coupled patches correspond to high values in the model resolution matrix (Figs 3b and d), indicating that the plate coupling is high where coupling is well-resolved by the data. We observe along-strike variation in the coupling ratio over these five regions. The westernmost and two easternmost regions exhibit higher coupling with respect to the two central regions, indicating likely segmentation of the Makran megathrust with varying coupling from west to east (Fig. 3). This pattern is consistent with previous coupling estimates of the MSZ that suggested that the western and eastern segments have higher coupling (∼58 per cent), while the central segment is weakly coupled (∼31 per cent, Frohling & Szeliga 2016). Distributed high coupling extends below 20-km depth in our model. However, we find these estimates to likely be an artifact of the distribution of surface observations given that the model resolution matrix exhibits low values over the corresponding fault areas. Moreover, historic reviews of Makran seismicity suggest that, with the exception of intermediate depth normal faulting earthquakes, nearly all recorded earthquakes occur at depths shallower than 20 km (Jackson & McKenzie 1984; Byrne *et al.* 1992), further suggesting that this downdip 'smear' of high coupling is likely unreal, but rather an artifact resulting from the lack of GPS observations in the vicinity of the fault areas.

3 COUPLING-BASED EARTHQUAKE SCENARIOS

3.1. Model resolution

After undertaking inversions of the GPS observations for back slip rates, we explore the potential characteristics of back slip that cannot be resolved by the sparsely located geodetic measurements. An

inverse model ($\boldsymbol{m}_{\mathbf{est}}$) of back-slip rate (or fault slip, more generally) only reveals what aspects of the true, underlying back-slip rate distribution ($\boldsymbol{m}_{\mathbf{true}}$) can be resolved given the location and quality of data, the imposed fault model (location, discretization), the imposed Earth structure, inversion regularization, and other sources of epistemic uncertainty. The resolution capabilities of an inverse problem need to be assessed in order to characterize the full range of potential underlying, true scenarios. Model resolution matrix ($\boldsymbol{R}_{\mathbf{m}}$) gives what a true model looks like with the available data collection strategy.

We use the model resolution matrix to interrogate this relationship between our inverted back-slip rate distributions ($\boldsymbol{m}_{\mathbf{est}}$) and the unknown true back-slip rate distribution ($\boldsymbol{m}_{\mathbf{true}}$) in order to define a suite of possible true back-slip rate distributions. The relationship between the true underlying back-slip rate model ($\boldsymbol{m}_{\mathbf{true}}$) and the inverted, estimated back-slip rate model ($\boldsymbol{m}_{\mathbf{est}}$) is

$$\boldsymbol{m}_{\mathbf{est}} = \boldsymbol{R}_{\mathbf{m}}\boldsymbol{m}_{\mathbf{true}}. \tag{6}$$

Using eq. (6) and our inverted back-slip rate model ($\boldsymbol{m}_{\mathbf{est}}$), we can then multiply any conjured, theoretical coupling scenario by the model resolution matrix, and then compare the output to our inverted coupling models and determine if the theoretical coupling scenario is possible given the model resolution. Fig. 4 illustrate the relationship between $\boldsymbol{R}_{\mathbf{m}}$, $\boldsymbol{m}_{\mathbf{est}}$ and $\boldsymbol{m}_{\mathbf{true}}$.

To construct different scenarios of $\boldsymbol{m}_{\mathbf{true}}$, we first divide the megathrust into three segments as previously described by varying coupling ratio (Fig. 3). We create in total of six back-slip rate scenarios on either one or multiple segments: east-only (E), central-only (C), west-only (W), east-central (EC), west-central (WC), and whole-fault (WCE). For each scenario, we assume that the interseismic back-slip rate extends to the trench and assign a series of combinations of downdip width and back-slip rate ($\boldsymbol{m}_{\mathbf{true}}$). Since there is little information on the downdip limit of plate coupling, and the model resolution is low at depth (Fig. 3), we keep the downdip widths as narrow as possible. Therefore, the downdip widths estimated in this study reflect the shallowest plate-coupling limits that can be constrained by the GPS data. We then multiply $\boldsymbol{m}_{\mathbf{true}}$ by the $\boldsymbol{R}_{\mathbf{m}}$ from our viscoelastic inversion to calculate how the back-slip rate distribution would be resolved after the inversion ($\boldsymbol{m}_{\mathbf{rsv}}$). In a trial-and-error manner, we calculate the root-mean-square error (RMSE) between $\boldsymbol{m}_{\mathbf{rsv}}$ and the inversion result $\boldsymbol{m}_{\mathbf{est}}$ to access whether the prescribed back-slip rate scenarios, under given model resolution, can produce the same back-slip rate pattern as the GPS inversion. Additionally, we conduct visual inspections to assess the fit between $\boldsymbol{m}_{\mathbf{rsv}}$ and $\boldsymbol{m}_{\mathbf{est}}$ within the ruptured segment(s) to ensure that actual back-slip rates are being fit, rather than noises (i.e. the downdip artifact shown in Fig. 3).

After obtaining different scenarios of $\boldsymbol{m}_{\mathbf{true}}$, we divide them by the plate convergence rate at the trench to calculate the corresponding plate-coupling models. For each scenario, we use an earthquake scaling relationship to estimate an earthquake moment magnitude. This moment magnitude corresponds to a possible future earthquake where the entire coupled segment(s) is ruptured. We use the scaling relationship between fault area and magnitude described in Allen & Hayes (2017), which is developed based on earthquakes in subduction zone and offshore environments:

$$\log(\mathrm{FA}) = a + b \times M_{\mathrm{w}}, \tag{7}$$

where M_{w} is the moment magnitude, FA is fault area in square kilometres, and a and b are regression coefficients that are set to be -3.63 and 0.96, respectively. After solving for the seismic moment magnitude, we calculate the coseismic uniform slip magnitude following

$$m_{\mathrm{o}} = DA\mu, \tag{8}$$

where m_{o} is the seismic moment release, D is the uniform fault slip, A is the summation of areas of all fault patches above the downdip limit and μ is shear modulus fixed at 40 GPa.

We further investigate scenarios where interseismic back-slip rate does not extend to the trench, but starts at certain depth downdip. To do this, for each scenario, we test combinations of back-slip rate and upper coupling depth limit while keeping the lower limit the same as before, and look for the best-fitting back-slip rate case, whose corresponding plate-coupling model and future earthquake slip magnitude are calculated following the same procedure as before.

3.2. Coupling-based earthquake scenarios: results

Figs 5 and 6 show the best-fitting plate-coupling models for all six back-slip rate scenarios under trench slip and blind slip conditions, respectively. Supporting Information Table S2 summarizes the source parameters for each back-slip rate scenario and the corresponding future earthquake. We observe several characteristics for different plate-coupling cases. In general, back-slip rate scenarios where locking extends to the trench produce trench-rupturing earthquakes of higher magnitudes than their blind-rupturing counterparts. For example, if the interseismic strain accumulation is released through an earthquake on the east-central segments, the magnitude of the earthquake is 9.0 and 8.7, under trench rupture and blind rupture conditions, respectively. We observe that single-segment coupling models, after being multiplied by the model resolution matrix, yield better fits to the GPS-inverted coupling model than the multisegment models within the corresponding segments. For instance, the east-only coupling model shows lower residuals than the whole-fault case within the eastern segment. Single-segment ruptures also produce lower magnitude than multisegment ruptures. Our results suggest that the Makran megathrust may be able to produce earthquakes up to M_{w} 8.7 for single-segment rupture, and M_{w} 9.2 for multisegment rupture. Additionally, the plate-coupling distributions for the east-only, central-only, and west-only back-slip rate cases indicate higher coupling in the eastern (50–60 per cent) and western (60–70 per cent) segments than the central segment (30–35 per cent, Fig. 7), which is again consistent with the results from Frohling & Szeliga (2016). Finally, when comparing the misfit between the GPS data and the forward-predicted velocities, we find that the prescribed back-slip scenarios yield good fit to data at stations close to the coupled patches. However, the westmost station exhibit large misfit exceeding the GPS uncertainty. This could result either from the spatially variable coupling on the western section or bias in the GPS velocity associated with the right-lateral motion on the nearby Minab–Zendan fault system.

4 TSUNAMI SIMULATIONS IN THE WESTERN INDIAN OCEAN

4.1. Tsunami simulations in the western Indian Ocean: methods

For each earthquake slip scenario, we calculate co-seismic ground/seafloor vertical displacements using *Pylith*. We use the same subduction zone geometry as before with the lower wedge exhibiting Maxwell rheology. We prescribe the slip distributions

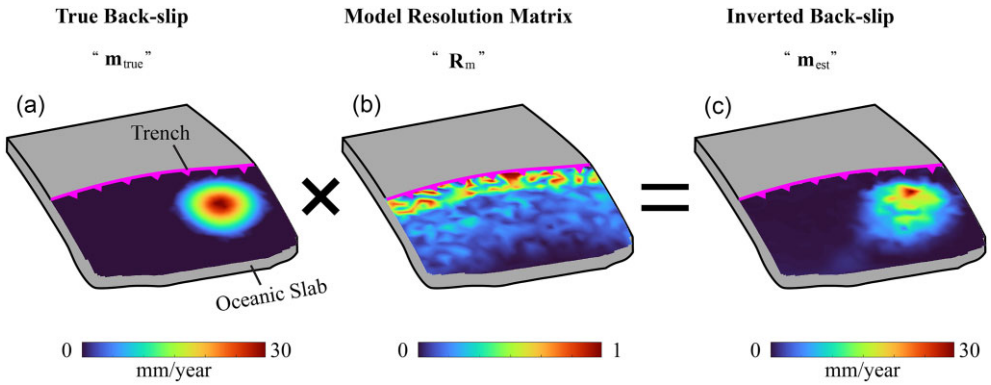

Figure 4. A general illustration of relationship between true back-slip rate ($\boldsymbol{m}_{\mathbf{true}}$), model resolution matrix ($\boldsymbol{R}_{\mathbf{m}}$) and inverted back-slip rate ($\boldsymbol{m}_{\mathbf{est}}$) in back-slip rate inversion on a subduction interface. The model resolution matrix in this figure is constructed based on synthetic GPS velocities that are equally spaced on both land and seafloor.

onto the megathrust and simulate the co-seismic surface static vertical displacements. Supporting Information Fig. S5 shows the resulting ground/seafloor uplift patterns. We then input these surface vertical displacements as initial condition for tsunami simulations using the open-source tsunami modelling code *GeoClaw* (http://www.clawpack.org/geoclaw). We ignore the time-dependent co-seismic slip evolution and assume that the earthquakes instantly deform the seafloor, as earthquake rupture propagates much faster than tsunami wave. We use the SRTM15 + relief model resampled at 1-arcminute pixel resolution for both topography and bathymetry inputs (Tozer *et al.* 2019). *GeoClaw* solves 2-D shallow water equations with finite volume technique (LeVeque *et al.* 2011), and employs adaptive mesh refinement (AMR) which automatically refines regions of higher tsunami complexity to finer mesh size according to user inputs. We use two levels of grid refinement with the coarsest set at 2-arcminute and the finest at 1-arcminute for the topography/bathymetry data set. For each earthquake scenario, we drive the tsunami simulation for 12 hours following the rupture. We then output time-series of estimated tsunami amplitudes (ETA) at 20 virtual tide gauges outside major port cities along coastlines bounding the Oman sea, the Strait of Hormuz, and southwestern Indian Ocean basin. Since the gauge points are located at different water depths, we apply Green's law to rescale the ETA to a common reference depth of 1 m following (Small & Melgar 2021).

4.2. Tsunami simulations in the western Indian Ocean: results

Fig. 8 illustrates the maximum tsunami wave heights calculated at the 20 tide gauge points for all six rupture scenarios under trench rupture and blind rupture conditions, respectively. Supporting Information Tables S3 and S4 summarize the maximum and peak-to-peak tsunami wave height results. In general, we observe spatial variation in the maximum and peak-to-peak tsunami wave heights in different regions of the western Indian Ocean basin. Fig. 9 shows the modelled ETA time-series resulting from the M_w 9.2 whole-fault trench-rupturing earthquake, and Fig. 10 shows the corresponding tsunami snapshots. We group the gauge points into four spatial domains with variable maximum wave height ranges: the northern Arabian Sea region, the west coast of India, eastern Africa, and the Strait of Hormuz. Following the M_w 9.2 rupture, coastal cities in the northern Arabian Sea region, including Muscat, Chah Bahar, Gwadar, Pasni, and Ormara, and Karachi, experience the most tsunami hazard with the maximum wave height reaching 2-5 m and peak-to-peak wave height reaching 4-9 m (Supporting Information Tables S3 and S4). Cities on the west coast of India (i.e. Surat, Mumbai, Mangalore, Kozhikode, and Kochi) are less affected, with wave height reaching 1–1.5 m (peak-to-peak: 1-3 m). Coastal cities bounding eastern Africa (i.e. Mogadishu, Dar es Salaam, Maputo, and Durban), and the Strait of Hormuz (i.e. Kuwait City, Dammam, Doha, Abu Dhabi, Dubai), are the least affected, with the incoming maximum and peak-to-peak wave height less than 1 m.

5 DISCUSSION

5.1. Seismic potential of the Makran megathrust

Our preferred plate-coupling model (Fig. 7) suggests that coupling varies along the strike of the subduction zone. We divide the MSZ into three regions based on the average coupling ratio, which are spatially similar to the three segments defined by Frohling & Szeliga (2016). The eastern segment, spanning from west of Pasni, Pakistan (63.2°E) to the eastern end of the domain (66.2°E), exhibits approximately 50 per cent coupling. This region hosted the 1945 M_w 8.0–8.3 megathrust earthquake (Byrne *et al.* 1992). The central segment spans from west of Chah Bahar, Iran (60°E) to the west of Pasni (63.2°E) and shows a reduced plate coupling of ∼30 per cent. Historically, this section of the fault has experienced few major earthquakes, with only two coastal events recorded in 1851 and 1864 (Fig. 1). Lastly, the western segment, from west of Chah Bahar (60°E) to the western end of the domain (57.2°E), is approximately 60 per cent coupled. However, the coupling of this segment is not well-resolved when compared to the other two segments, as the back-slip rate inversion is noisy downdip of the regional seismogenic zone. This likely results from low GPS station coverage in the region, or neglecting the stress partitioning contributed by the Minab–Zendan fault system to the west.

Segmentation of the megathrust implies variation in degree of earthquake hazard potential along the MSZ. Following the asperity model of Lay & Kanamori (1981), strong plate coupling corresponds to larger asperity size and is more likely to produce larger events, whereas weak coupling indicates smaller asperity size and likely results in smaller events. Higher plate coupling is also an indication of faster interseismic strain accumulation on the megathrust, where subduction zone earthquakes

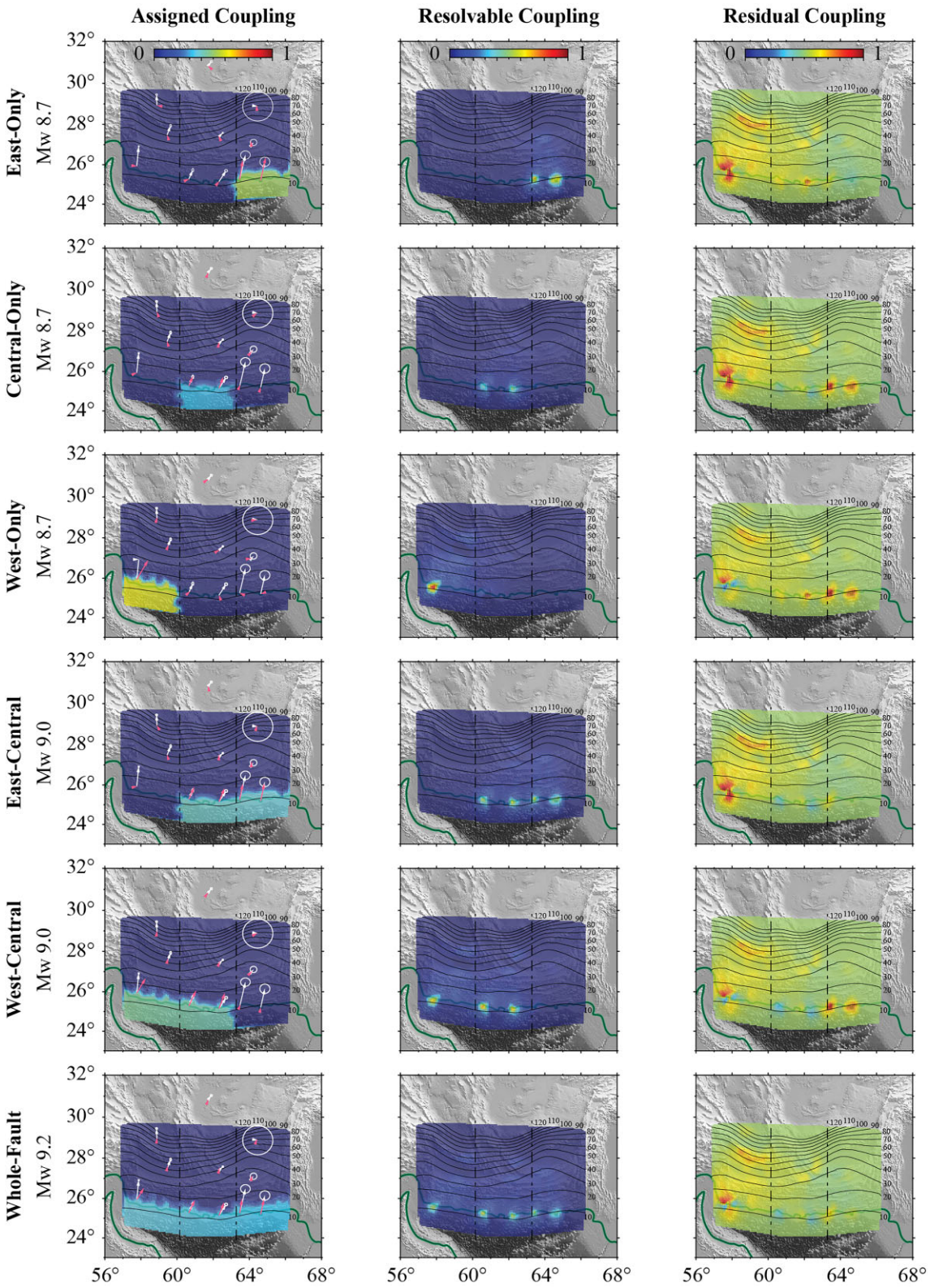

Figure 5. Best-fitting single- and multisegment plate-coupling scenarios and the corresponding earthquake magnitudes under the trench slip condition. The first column shows the assigned plate coupling corresponding to each back-slip rate case. The second column shows the resolvable coupling (multiply the first column by the corresponding model resolution matrix). The third column shows the residual between the resolvable coupling and the inverted coupling shown in Fig. 3. Each moment magnitude corresponds to an earthquake for the given coupling scenario assuming that the interseismic strain accumulation is fully released. White and pink arrows in the first column correspond to GPS velocity data and forward-predicted velocities, respectively.

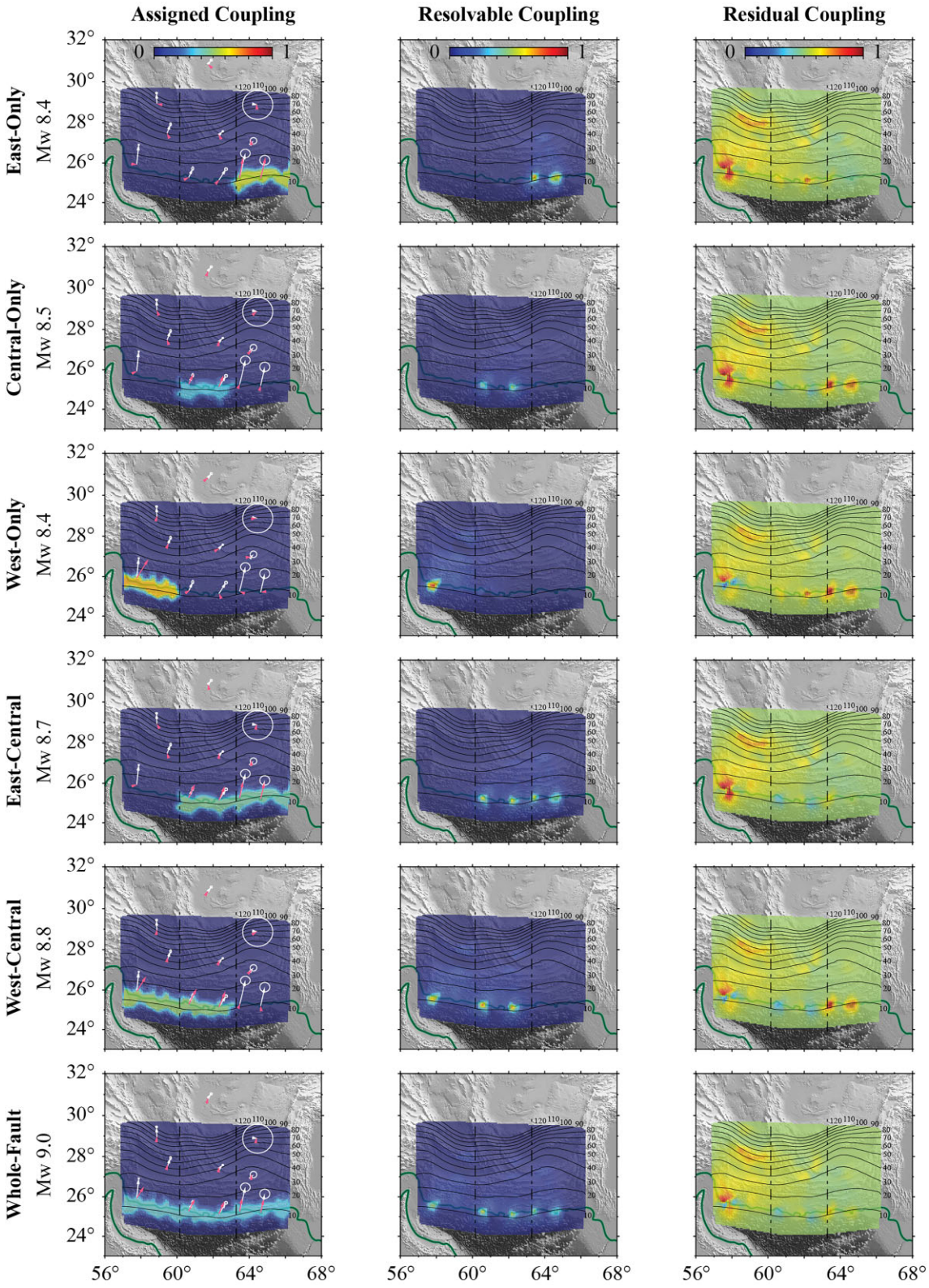

Figure 6. Best-fitting single- and multisegment plate-coupling scenarios and the corresponding earthquake magnitudes under the blind slip condition.

yield shorter recurrence intervals than those of the same magnitudes but produced on weakly coupled plate interfaces. We calculate the recurrence intervals for all earthquake scenarios by dividing the uniform co-seismic slip magnitudes by the back-slip rates (Supporting Information Table S2). The results show that, under trench-rupture condition, the recurrence intervals for an M_w 8.7 earthquake that ruptures the eastern, central and western segments are approximately 373, 664 and 381 yr, respectively, with unknown uncertainties. This change in recurrence interval correlates to the variation in plate coupling from east to west, where the

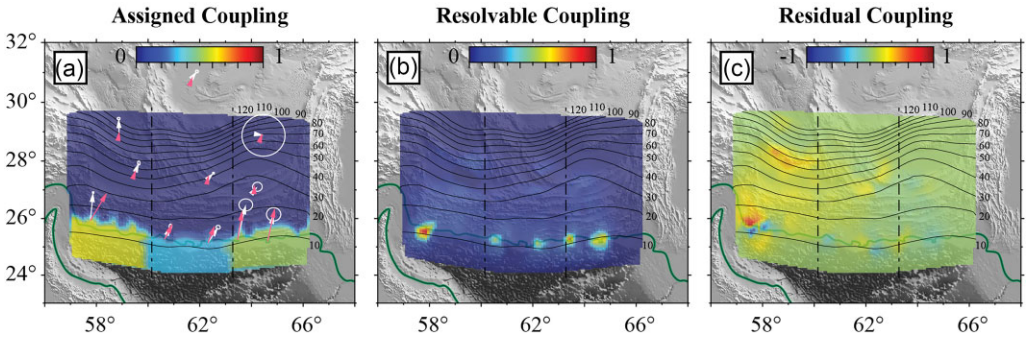

Figure 7. The preferred coupling model of the Makran megathrust and its resolvability by the GPS data.

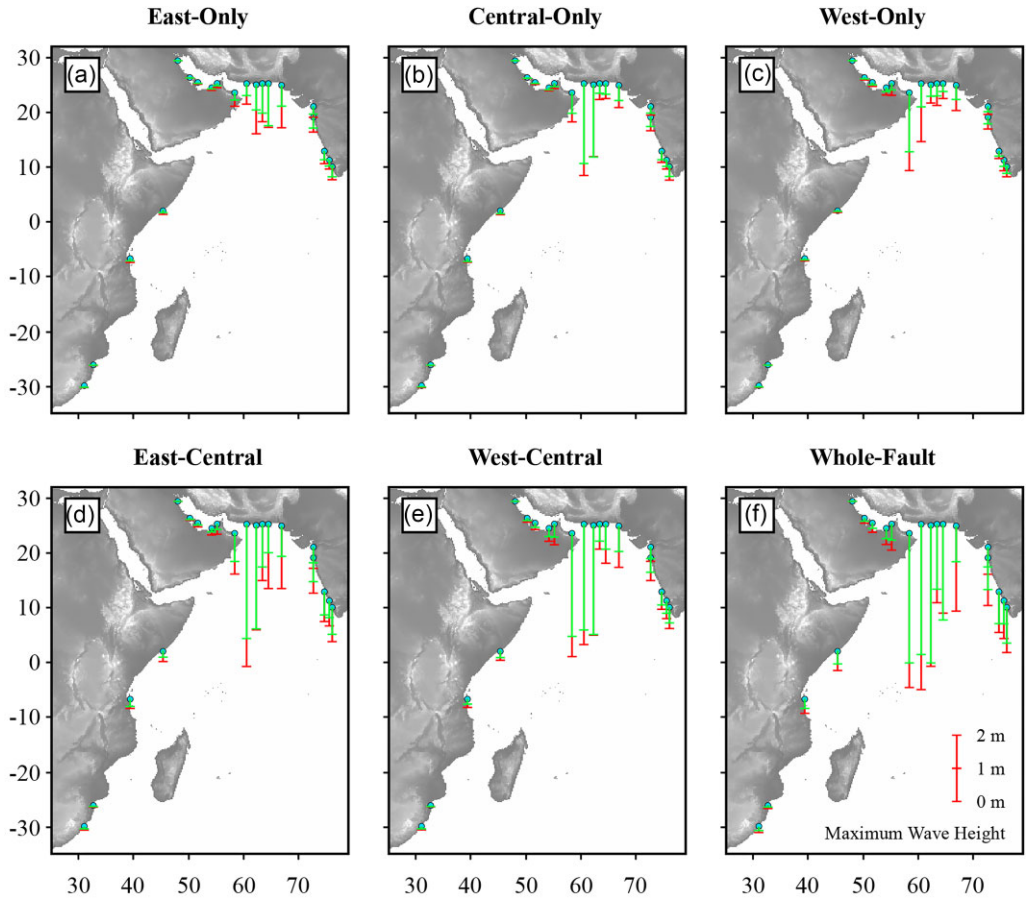

Figure 8. Maximum tsunami wave heights at 20 synthetic gauge points (cyan circles) following single- and multisegment trench rupturing (red) and blind (green) earthquakes.

eastern and western segments are stronger coupled than the central segment, resulting in shorter recurrence intervals for earthquakes of a given magnitude. Therefore, the eastern and western Makran are likely able to host larger, more frequent earthquake events than the central Makran.

5.2. Tsunami hazard potential in the western Indian Ocean basin

Our coupling-based tsunami simulation indicates variations in expected tsunami wave height along the coastline bounding the western Indian Ocean basin. In the largest earthquake scenario where the entire megathrust is rupture to the trench, the northern Arabian Sea region experiences the most severe tsunami hazard with the maximum wave height reaching several coastal cities at 2–5 m within the first hour after the earthquake (Supporting Information Table S3, Figs 9 and 10). The peak tsunami wave reduces to 1–1.5 m height and arrives at the west coast of India after 4 hr. The east coast of Africa and the Strait of Hormuz are the least affected by the M_w 9.2 earthquake in Makran, where the incoming maximum wave height is less than 1 m. For all 20 virtual gauge points, we define and calculate a simple index, termed the tsunami hazard score (THS), to assess the tsunami hazard potential at each location considering all 12 possible earthquake scenarios in Makran. The THS is defined as the weighted sum of number of events exceeding given maximum tsunami wave height thresholds at a gauge point for all 12

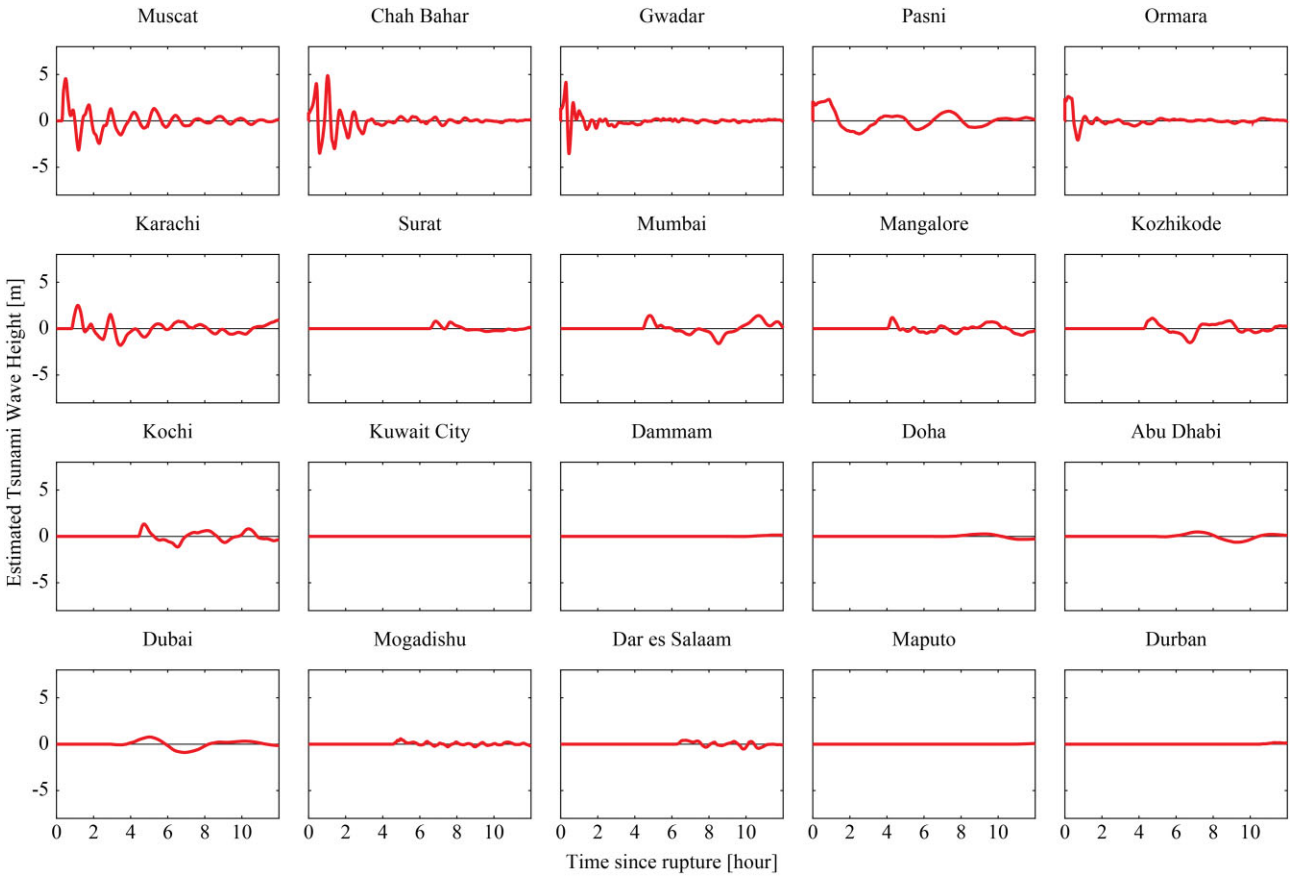

Figure 9. Modelled tsunami wave height time-series at gauge points offshore major coastal cities in the western Indian Ocean region following the M_w 9.2 whole-fault trench-rupturing earthquake.

earthquake events, normalized between 0 and 100:

$$\mathrm{THS} = \sum_{i=1}^{12} W_i N_i, \tag{9}$$

where N_i is the number of events producing maximum wave height larger than W_i metres (from 1 to 4.5 m, 0.5-m increment). Supporting Information Table S5 shows the THS summary for all 20 coastal cities. Again, cities in the northern Arabian Sea region yield the highest THS (i.e. having the highest tsunami potential from earthquakes in Makran). Coastal cities in western India yield lower THS values, and cities in eastern Africa and the Strait of Hormuz have the lowest score. Specifically, Muscat, Char Bhar and Gwadar are the three cities with highest THS values. Muscat is the capital and the most populated city in Oman. Char Bhar and Gwadar are the two of the fastest-growing commercial port cities in the region. Tsunami events of maximum wave height of 3–5 m at these locations can cause severe destruction to coastal infrastructures and port facilities, and result in significant human casualties and economic losses.

Tsunami height records and observations in the Makran are incomplete. The 1945 M_w 8.0–8.3 earthquake is the first instrumentally recorded event, and the only event for which observations of tsunami wave heights along different coasts are available (Heidarzadeh *et al.* 2008). According to Berninghausen (1966), the wave heights were at about 12–15 m at Pasni and Ormara, and 1.4 m at Karachi. Ambraseys & Melville (2005) reported the wave height to be about 4–5 m in Pasni and 1.5 m in Karachi. Adams *et al.* (2018) detided a Karachi tide-gauge record and reported the water level to be ∼0.5 m above ambient tide. Page *et al.* (1979) reported a wave height reaching 7–10 m along several parts of the Makran coast. Since the 1945 earthquake ruptured in the eastern segment of the megathrust, we compare our predicted maximum tsunami wave heights from the east-only trench-rupture scenario to the field observations. Our model suggests a maximum wave height of 1.28 m in Karachi, which is in reasonable agreement with the field observations. However, the wave height predictions at Pasni and Ormara are much lower (1.15 and 1.32 m, respectively) than the 12–15 m reported by previous studies. This discrepancy between modelling results and field observations is consistent with other numerical models of this earthquake (Heidarzadeh *et al.* 2008; Heidarzadeh & Satake 2015; Qiu *et al.* 2022). Heidarzadeh *et al.* (2008) proposed three possible explanations for this discrepancy: (1) the reports of 12–15 m wave heights were incorrect and an exaggeration; (2) the large wave heights resulted from submarine landslides triggered by the earthquake; and (3) the elevated wave heights could be produced by large displacements on splay faults near the trench, which are not considered in our models. Qiu *et al.* (2022) conducted tsunami simulations of the 1945 megathrust rupture with additional displacements on splay faults. Their results indicate amplification of tsunami wave height when considering the presence of splay faults.

6 CONCLUSIONS

Although we cannot currently resolve megathrust coupling in the MSZ with the resolution that can be accomplished in other global subduction zones, this study serves to provide a synopsis of what is

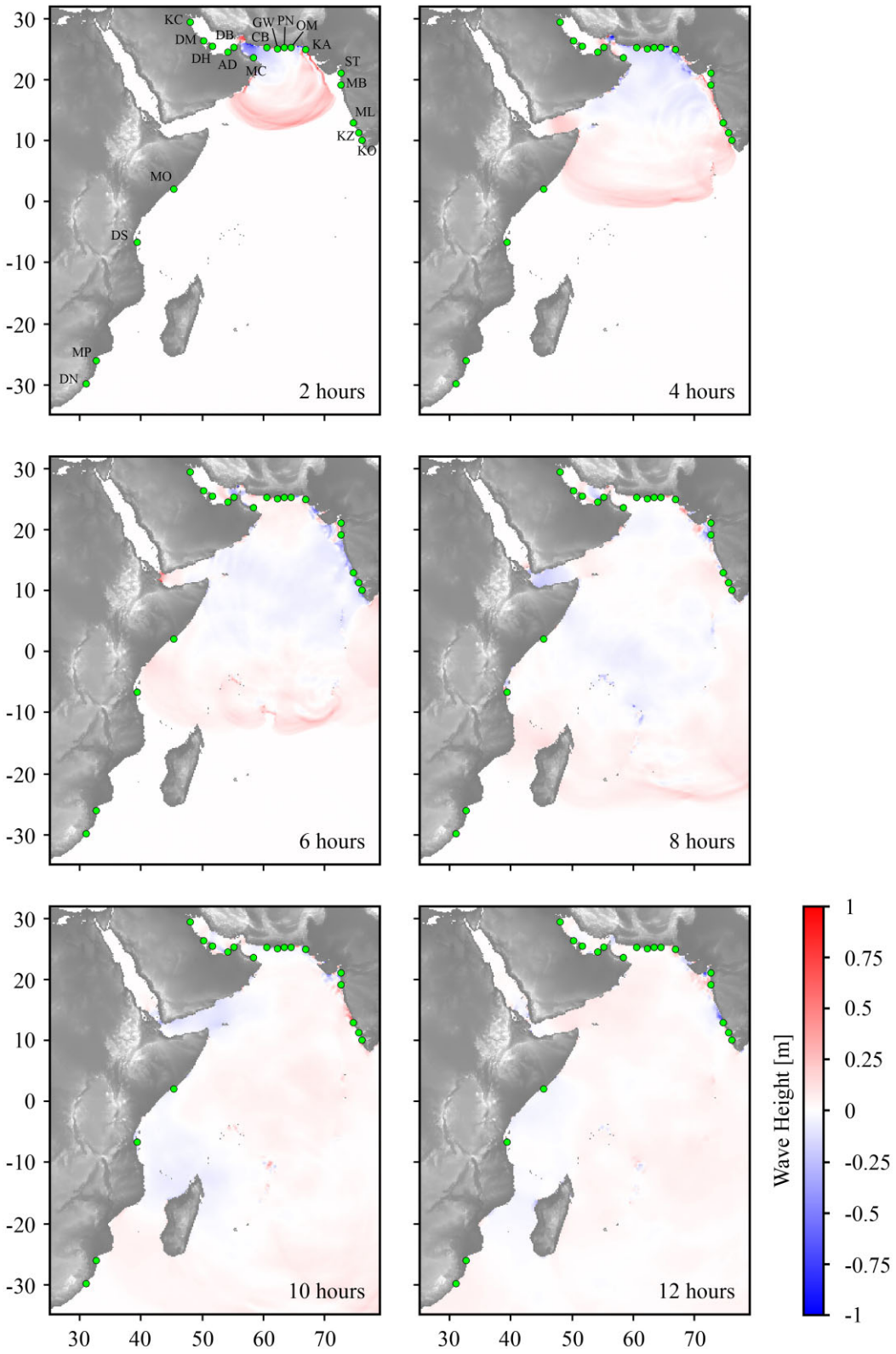

Figure 10. Modelled tsunami wave propagation after the M_w 9.2 whole-fault trench-rupturing earthquake. Solid circles indicate gauge point locations offshore major coastal cities.

possible given our current data availability. By developing coupling scenarios that are consistent with the model resolution of our inverse problem, we are able to hypothesize several important characteristics of coupling in the MSZ and how future great earthquakes may play out:

(i) The plate-coupling distribution that can be directly inferred from available GPS observations is insufficient to uniquely explain the history of great earthquakes in the Makran; thus, there is significant coupling that cannot be directly resolved with current observations.

(ii) The megathrust of the MSZ is likely segmented with variable plate coupling along strike, in agreement with previous studies. The eastern and western segments correspond to approximately 50 and 60 per cent coupling, respectively. The central segment exhibits lower coupling (about 30 per cent) than the other two segments.

(iii) Our investigation suggests that, based on the inverted plate coupling, the Makran megathrust may be able to produce earthquakes up to M_w 8.7 for single-segment rupture, and M_w 9.2 for multisegment rupture.

(iv) Population centres along the western Indian Ocean basin may be exposed to tsunami hazard as a result of Makran great earthquakes. The northern Arabian Sea region experiences the most severe tsunami hazard with the maximum wave height reaching several coastal cities at 2–5 m. The west coast of India is less affected with wave height reduced to 1–1.5 m. The east coast of Africa and the Strait of Hormuz are the least affected, for which the incoming wave height is less than 1 m.

SUPPORTING INFORMATION

Supplementary data are available at *GJI* online.

Fig. S1. Inverted plate-coupling models using (a) minimum moment and (b) Laplacian regularization.

Fig. S2. Inverted interseismic viscoelastic plate-coupling models of the Makran megathrust and the diagonal components of the model resolution matrices using varying smoothing coefficient. White arrows: GPS velocity data; Pink arrows: forward-predicted velocity from the inversion; Black solid lines: contours of the plate interface marked by depth in kilometer; Black dash lines: boundaries between different fault segments. Dark green lines: coastlines.

Fig. S3. Example of 3 nonoverlapping fault patches for inversion approach. When calculating the surface deformation resulting from slipping of each patch, we apply unit slip to the nodes located in the patch of interest while applying zero slip to all the other nodes on the fault.

Fig. S4. Misfit between the observed and predicted GPS velocities using different rake values in the back-slip rate inversion.

Fig. S5. Co-seismic static ground/seafloor vertical displacements resulting from single- and multi-segment earthquakes under both trench rupture and blind rupture conditions.

Table S1. Four model domains and their material properties used in the generation of Green's functions for both elastic and viscoelastic models.

Table S2. Source parameters for all back-slip scenarios and the corresponding future earthquake cases.

Table S3. Maximum tsunami wave height response (in meters) at the 20 tide gauge points (cities) resulting from 12 rupture scenarios under both trench rupture and blind rupture conditions.

Table S4. Peak-to-peak tsunami wave height response (in meters) at the 20 tide gauge points (cities) resulting from 12 rupture scenarios under both trench rupture and blind rupture conditions.

Table S5. Occurrence of events larger than certain maximum wave height thresholds and Tsunami Hazard Score (THS) at the 20 tide gauge points (cities).

Please note: Oxford University Press is not responsible for the content or functionality of any supporting materials supplied by the authors. Any queries (other than missing material) should be directed to the corresponding author for the paper.

ACKNOWLEDGMENTS

This work was supported by NSF Award EAR 1917500. High-performance computational resources were provided by the University of Iowa, Iowa City. Any use of trade, firm or product names is for descriptive purposes only and does not imply endorsement by the U.S. Government.

DATA AVAILABILITY

The GPS velocity data used to invert for interseismic plate coupling were imported from Frohling & Szeliga (2016). Several figures were generated using the Generic Mapping Tool (Wessel *et al.* 2013).

REFERENCES

Aagaard, B.T., Knepley, M.G. & Williams, C.A. 2013. A domain decomposition approach to implementing fault slip in finite-element models of quasi-static and dynamic crustal deformation. *J. geophys. Res.,* **118**(6), 3059–3079.

Abdollahi, S., Ardestani, V.E., Zeyen, H. & Shomali, Z.H. 2018. Crustal and upper mantle structures of Makran subduction zone, SE Iran by combined surface wave velocity analysis and gravity modeling. *Tectonophysics,* **747–748,** 191–210.

Adams, L.M., Atwater, B.F. & Hasan, H. 2018. Karachi tides during the 1945 Makran tsunami. *Geosci. Lett.,* **5**(1), 25. doi: 10.1186/s40562-018-0121-z.

Allen, T.I. & Hayes, G.P. 2017. Alternative rupture-scaling relationships for subduction interface and other offshore environments. *Bull. seism. Soc. Am.,* **107**(3), 1240–1253.

Altamimi, Z., Collilieux, X. & Métivier, L. 2011. ITRF2008: an improved solution of the international terrestrial reference frame. *J. Geod.,* **85**(8), 457–473.

Altamimi, Z., Métivier, L. & Collilieux, X. 2012. ITRF2008 plate motion model. *J. geophys. Res.,* **117**(B7). doi: 10.1029/2011JB008930.

Ambraseys, N.N. & Melville, C.P. 2005. *A History of Persian Earthquakes*. Cambridge Univ. Press.

Baptista, M.A., Miranda, J.M., Omira, R. & El Hussain, I. 2020. Study of the 24 September 2013 Oman Sea tsunami using linear shallow water inversion. *Arabian Journal of Geosciences,* **13**(14), 606. doi: 10.1007/s12517-020-05632-z.

Barnhart, W.D., Hayes, G.P., Samsonov, S.V., Fielding, E.J. & Seidman, L.E. 2014. Breaking the oceanic lithosphere of a subducting slab: the 2013 Khash, Iran earthquake. *Geophys. Res. Lett.,* **41**(1), 32–36.

Barnhart, W.D. & Lohman, R.B. 2010. Automated fault model discretization for inversions for coseismic slip distributions. *J. geophys. Res.,* **115**(B10). doi: 10.1029/2010JB007545.

Berninghausen, W.H. 1966. Tsunamis and seismic seiches reported from regions adjacent to the Indian Ocean. *Bull. seism. Soc. Am.,* **56**(1), 69–74.

Burg, J.-P. 2018. Geology of the onshore Makran accretionary wedge: synthesis and tectonic interpretation. *Earth Sci. Rev.,* **185,** 1210–1231.

Byrne, D.E., Sykes, L.R. & Davis, D.M. 1992. Great thrust earthquakes and aseismic slip along the plate boundary of the Makran Subduction Zone. *J. geophys. Res.,* **97**(B1), 449–478.

Cheng, G., Barnhart, W.D. & Li, S. 2022. Power-law viscoelastic flow of the lower accretionary prism in the Makran subduction zone following the 2013 Baluchistan earthquake. *J. geophys. Res.,* **127**(11), e2022JB024493. doi: 10.1029/2022JB024493.

Craig, T.J. & Copley, A. 2014. An explanation for the age independence of oceanic elastic thickness estimates from flexural profiles at subduction zones, and implications for continental rheology. *Earth planet. Sci. Lett.,* **392,** 207–216.

DeMets, C., Gordon, R.G. & Argus, D.F. 2010. Geologically current plate motions. *Geophys. J. Int.,* **181**(1), 1–80.

Fowler, S.R., White, R.S. & Louden, K.E. 1985. Sediment dewatering in the Makran accretionary prism. *Earth planet. Sci. Lett.,* **75**(4), 427–438.

Frohling, E. & Szeliga, W. 2016. GPS constraints on interplate locking within the Makran subduction zone. *Geophys. J. Int.,* **205**(1), 67–76.

Harris, R.A. & Segall, P. 1987. Detection of a locked zone at depth on the Parkfield, California, segment of the San Andreas Fault. *J. geophys. Res.,* **92**(B8), 7945–7962.

Hayes, G.P., Moore, G.L., Portner, D.E., Hearne, M., Flamme, H., Furtney, M. & Smoczyk, G.M. 2018. Slab2, a comprehensive subduction zone geometry model. *Science,* **362**(6410), 58–61.

Heck, N.H. 1947. List of seismic sea waves∗. *Bull. seism. Soc. Am.,* **37**(4), 269–286.

Heidarzadeh, M., Pirooz, M.D., Zaker, N.H., Yalciner, A.C., Mokhtari, M. & Esmaeily, A. 2008. Historical tsunami in the Makran subduction zone off the southern coasts of Iran and Pakistan and results of numerical modeling. *Ocean Eng.,* **35**(8), 774–786.

Heidarzadeh, M. & Satake, K. 2015. New insights into the source of the Makran tsunami of 27 November 1945 from tsunami waveforms and coastal deformation data. *Pure appl. Geophys.,* **172**(3), 621–640.

Herring, T.A., King, R.W. & McClusky, S.C. 2010a. GAMIT reference manual, GPS analysis at MIT release 10.4. Tech. Rep., Dept. Earth Atmos. Planet. Sci. Mass. Inst. Technol., Cambridge, MA.

Herring, T.A., King, R.W. & McClusky, S.C. 2010b. GLOBK: global Kalman filter VLBI and GPS analysis program, release 10.4. Tech. Rep., Dept. Earth Atmos. Planet. Sci. Mass. Inst. Technol., Cambridge, MA.

Hoffmann, G., Grützner, C., Reicherter, K. & Preusser, F. 2015. Geoarchaeological evidence for a Holocene extreme flooding event within the Arabian Sea (Ras al Hadd, Oman). *Quat. Sci. Rev.,* **113,** 123–133.

Hu, Y., Wang, K., He, J., Klotz, J. & Khazaradze, G. 2004. Three-dimensional viscoelastic finite element model for postseismic deformation of the great 1960 Chile earthquake. *J. geophys. Res.,* **109**(B12). doi: 10.1029/2004JB003163.

Jackson, J. & McKenzie, D. 1984. Active tectonics of the Alpine–Himalayan Belt between western Turkey and Pakistan. *Geophys. J. R. Astron. Soc.,* **77**(1), 185–264.

Kopp, C., Fruehn, J., Flueh, E.R., Reichert, C., Kukowski, N., Bialas, J. & Klaeschen, D. 2000. Structure of the Makran subduction zone from wide-angle and reflection seismic data. *Tectonophysics,* **329**(1), 171–191.

Lay, T. & Kanamori, H. 1981. An asperity model of large earthquake sequences, in *Earthquake Prediction,* pp. 579–592, American Geophysical Union (AGU). doi: 10.1029/ME004p0579.

LeVeque, R.J., George, D.L. & Berger, M.J. 2011. Tsunami modelling with adaptively refined finite volume methods∗. *Acta Numer.,* **20,** 211–289.

Li, S. & Chen, L. 2023. How long can the postseismic and interseismic phases of great subduction earthquake sustain? Toward an integrated earthquake-cycle perspective. *Geophys. Res. Lett.,* **50**(11), e2023GL103976. doi: 10.1029/2023GL103976.

Li, S., Fukuda, J. & Oncken, O. 2020. Geodetic evidence of time-dependent viscoelastic interseismic deformation driven by megathrust locking in the southwest Japan subduction zone. *Geophys. Res. Lett.,* **47**(4), e2019GL085551. doi: 10.1029/2019GL085551.

Li, S., Moreno, M., Bedford, J., Rosenau, M. & Oncken, O. 2015. Revisiting viscoelastic effects on interseismic deformation and locking degree: a case study of the Peru–North Chile subduction zone. *J. geophys. Res.,* **120**(6), 4522–4538.

Li, S., Wang, K., Wang, Y., Jiang, Y. & Dosso, S.E. 2018. Geodetically inferred locking state of the Cascadia megathrust based on a viscoelastic earth model. *J. geophys. Res.,* **123**(9), 8056–8072.

Lin, Y.N., Jolivet, R., Simons, M., Agram, P.S., Martens, H.R., Li, Z. & Lodi, S.H. 2015. High interseismic coupling in the Eastern Makran (Pakistan) subduction zone. *Earth planet. Sci. Lett.,* **420,** 116–126.

Maggi, A., Jackson, J.A., Priestley, K. & Baker, C. 2000. A re-assessment of focal depth distributions in southern Iran, the Tien Shan and northern India: do earthquakes really occur in the continental mantle? *Geophys. J. Int.,* **143**(3), 629–661.

Masterlark, T. 2003. Finite element model predictions of static deformation from dislocation sources in a subduction zone: sensitivities to homogeneous, isotropic, Poisson-solid, and half-space assumptions. *J. geophys. Res.,* **108**(B11). doi: 10.1029/2002JB002296.

Menke, W. 2018. *Geophysical Data Analysis: Discrete Inverse Theory*. Academic Press.

Mokhtari, M., Ala Amjadi, A., Mahshadnia, L. & Rafizadeh, M. 2019. A review of the seismotectonics of the Makran subduction zone as a baseline for tsunami hazard assessments. *Geosci. Lett.,* **6**(1), 13. doi: 10.1186/s40562-019-0143-1.

Musson, R.M.W. 2009. Subduction in the Western Makran: the historian's contribution. *J. Geol. Soc.,* **166**(3), 387–391.

Okada, Y. 1992. Internal deformation due to shear and tensile faults in a half-space. *Bull. seism. Soc. Am.,* **82**(2), 1018–1040.

Page, W.D., Alt, J.N., Cluff, L.S. & Plafker, G. 1979. Evidence for the recurrence of large-magnitude earthquakes along the Makran coast of Iran and Pakistan. *Tectonophysics,* **52**(1), 533–547.

Peterson, K.E., Barnhart, W.D. & Li, S. 2018. Viscous accretionary prisms: viscoelastic relaxation of the Makran accretionary prism following the 2013 Baluchistan, Pakistan earthquake. *J. geophys. Res.,* **123**(11), 10 107–10 123.

Platt, J.P., Leggett, J.K., Young, J., Raza, H. & Alam, S. 1985. Large-scale sediment underplating in the Makran accretionary prism, southwest Pakistan. *Geology,* **13**(7), 507–511.

Qiu, Q., Zhou, Z., Lin, J., Zhang, F., Chen, Z. & Yang, X. 2022. Great earthquake and tsunami potential in the eastern Makran subduction zone: new insights from geodetic and structural constraints. *Tectonophysics,* **837,** 229462.

Quittmeyer, R.C. & Jacob, K.H. 1979. Historical and modern seismicity of Pakistan, Afghanistan, northwestern India, and southeastern Iran. *Bull. seism. Soc. Am.,* **69**(3), 773–823.

Rajendran, C.P., Rajendran, K., Shah-hosseini, M., Beni, A.N., Nautiyal, C.M. & Andrews, R. 2013. The hazard potential of the western segment of the Makran subduction zone, northern Arabian Sea. *Nat. Hazards,* **65**(1), 219–239.

Regard, V. *et al.* 2010. The transition between Makran subduction and the Zagros collision: recent advances in its structure and active deformation. *Geol. Soc. London Spec. Publ.,* **330**(1), 43–64.

Savage, J.C. 1983. A dislocation model of strain accumulation and release at a subduction zone. *J. geophys. Res.,* **88**(B6), 4984–4996.

Shad Manaman, N., Shomali, H. & Koyi, H. 2011. New constraints on upper-mantle S-velocity structure and crustal thickness of the Iranian plateau using partitioned waveform inversion. *Geophys. J. Int.,* **184**(1), 247–267.

Small, D.T. & Melgar, D. 2021. Geodetic coupling models as constraints on stochastic earthquake ruptures: an example application to PTHA in Cascadia. *J. geophys. Res.,* **126**(7), e2020JB021149. doi: 10.1029/2020JB021149.

Smith, G., McNeill, L., Henstock, T.J. & Bull, J. 2012. The structure and fault activity of the Makran accretionary prism. *J. geophys. Res.,* **117**(B7). doi: 10.1029/2012JB009312.

Tozer, B., Sandwell, D.T., Smith, W.H.F., Olson, C., Beale, J.R. & Wessel, P. 2019. Global bathymetry and topography at 15 arc sec: SRTM15+. *Earth Space Sci.,* **6**(10), 1847–1864.

Wang, K., Hu, Y. & He, J. 2012. Deformation cycles of subduction earthquakes in a viscoelastic Earth. *Nature,* **484,** 327–332.

Wessel, P., Smith, W.H.F., Scharroo, R., Luis, J. & Wobbe, F. 2013. Generic Mapping Tools: improved version released. *EOS, Trans. Am. geophys. Un.,* **94**(45), 409–410.